

RESEARCH ARTICLE

10.1002/2013JB010877

Key Points:

- Earthquake catalog is relocated using local velocity model
- Seismicity collapses to certain zones while others became more spaced
- Earthquake clusters are defined and associated with previously mapped faults

Supporting Information:

- Readme
- Figure S1
- Table S1

Correspondence to:

N. Wetzler,
nadav.wetzler@gmail.com

Citation:

Wetzler, N., A. Sagy, and S. Marco (2014), The association of micro-earthquake clusters with mapped faults in the Dead Sea basin, *J. Geophys. Res. Solid Earth*, 119, 8312–8330, doi:10.1002/2013JB010877.

Received 16 DEC 2013

Accepted 14 SEP 2014

Accepted article online 17 SEP 2014

Published online 16 NOV 2014

The association of micro-earthquake clusters with mapped faults in the Dead Sea basin

Nadav Wetzler^{1,2}, Amir Sagy², and Shmuel Marco¹

¹Department of Geosciences, Tel Aviv University, Tel Aviv, Israel, ²Geological Survey of Israel, Jerusalem, Israel

Abstract About 1100 micro-earthquakes that occurred along the Dead Sea basin during the past 25 years express ongoing seismic activity along mostly obscured fault segments. We apply seismological and statistical methods in order to associate seismic activity with geological and geophysical data and to locate and characterize active fault segments in the basin; three regional 1-D velocity models and the double-difference method were used for the relocation of seismic events. Geostatistical analysis shows that in first order the micro-earthquakes reflect faulting along segments of the main longitudinal fault while seismic quiescence along historically active zones indicates locked segments and stress concentration. Based on waveform similarity, spatial and temporal proximity, we define earthquake clusters that comprise about 30% of the relocated seismicity and two thirds of the total seismic moment. About 80% of the clusters are associated with N-S trending faults. In two cases the clusters indicate a migration of the seismicity in time and space, one of which preceded the largest earthquake in our catalog ($M_{5.2}$). In addition to the associated longitudinal activity, several clusters appear to represent faulting in east-west orientation which is interpreted here as a secondary fault system.

1. Introduction

During the last decades seismology has become an essential tool for revealing fault structures across tectonically active zones [Chiaraluce *et al.*, 2003; Fukuyama *et al.*, 2003; Shearer *et al.*, 2005; Ouillon and Sornette, 2011; Kroll *et al.*, 2013]. In this study we address the seismic activity in the Dead Sea basin (DSB, Figure 1) to reveal the fault geometry in depth. The DSB is a deep depression that developed between two segments of the Dead Sea Transform (DST, Figure 1) along a left step-over between the Jordan Valley fault and the Arava fault [Garfunkel *et al.*, 1981; Garfunkel and Ben-Avraham, 1996]. The DSB has been active since the Miocene and has accommodated the majority of the total > 100 km left-lateral motion in this area [Garfunkel, 1981; 1997]. Several geophysical studies in the DSB reveal a partial picture of the crustal structure [e.g., ten Brink *et al.*, 1993; Ginzburg and Ben-Avraham, 1997; ten Brink *et al.*, 2006; Choi *et al.*, 2011; ten Brink and Flores, 2012]. Seismic reflection surveys in particular provide a tool for identifying faults within the top few kilometers of the upper crust [Neev and Hall, 1979; Kashai and Croker, 1987; Gardosh *et al.*, 1997; Ginzburg *et al.*, 2007]. However, in areas of a thick crust, such as the DSB, where seismicity reaches depths of 25 km [Aldersons *et al.*, 2003; Braeuer *et al.*, 2012], the continuation of faults into the basement and the deep seismogenic zone is poorly constrained. Furthermore, it is not clear how the lateral displacement of the transform motion is accommodated by the internal structure of the basin.

Several studies have identified earthquake clusters that were associated with mapped fault structures. van Eck and Hofstetter [1989] identified four spatial earthquake clusters that were associated with the main longitudinal faults: two in the south of the DSB, associated with the Eastern Border Fault (EBF) (Figure 2a), and two associated with the West Intrabasinal Fault (WIF) (Figure 2a). In addition, a 17 month microseismological study using a seismic array of 65 stations from the Dead Sea Integrated Research project at the southern DSB shows clustered activity at depths of ~20 km associated with the EBF and the WIF (Figure 2a) [Braeuer *et al.*, 2012]. However, the association of earthquake clusters was not limited only to the longitudinal faults. Hofstetter *et al.* [2007] recognized clustered activity north of the Lisan Peninsula that was associated with an E-W striking transverse fault. These seismological studies imply the possibility of localized cluster activity within the basin and manifest the association of some of these clusters with the mapped faults. Some of the clusters' activity cannot be explained directly by the fault geometry at the surface. One example is the 5.1 magnitude (M_w) earthquake of 11 February 2004. This event was followed by a linear

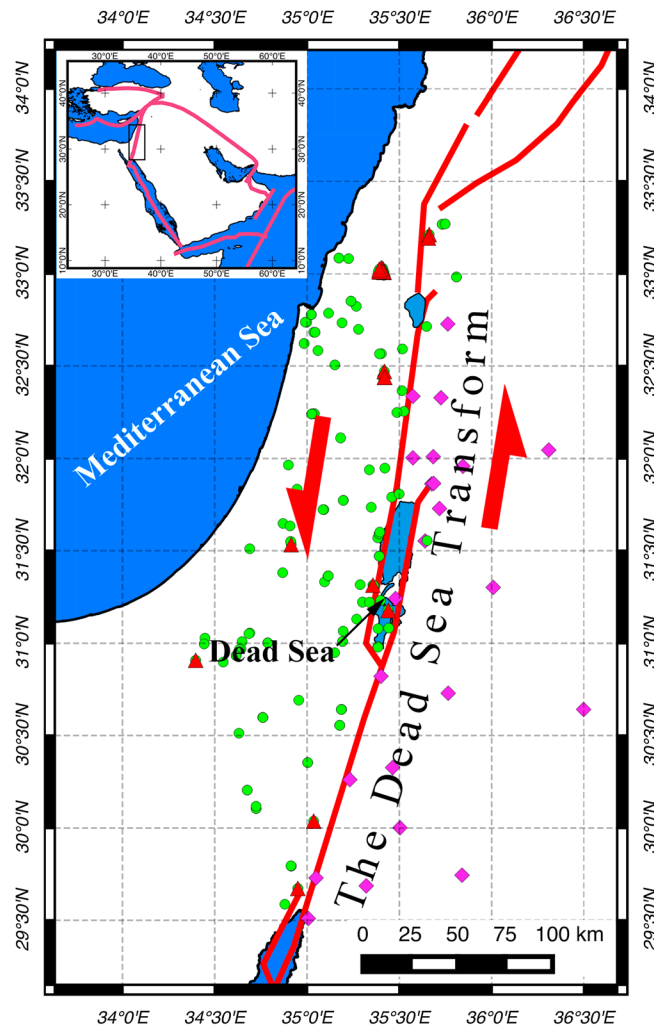


Figure 1. The regional seismic network including all operational stations between 1985 and 2010, including the Israel Seismic Network (green dots = short period and red triangles = broadband) and the Jordanian Seismic Observatory (purple diamonds). The Dead Sea Transform fault system is plotted in red lines, and red arrows show the relative slip motion. A wider map of the Middle East is inserted at the top left corner.

cluster at the northern tip of the basin that trends almost perpendicular to the main longitudinal faults [Hofstetter *et al.*, 2008].

In this study we associate the micro-earthquake activity with the mapped faults of the DSB. Due to the lithology variations in and outside the DSB [ten Brink and Flores, 2012], location of earthquakes is difficult. Therefore, we relocate the seismic activity within the DSB between 1985 and 2010 using the double-difference method. It has been shown that in many cases, second-order corrections provide significant improvement in earthquake locations. We show that the new locations are more clustered to specific zones in the basin while other parts of the basin show almost no seismicity. In addition to refining event locations, we use the relocated catalog to identify and analyze earthquake clustering. Clusters reflect local strain concentrations, which might be associated with faulting on one or more fault segments. Methods for detecting such clusters within a data set of vast seismic events include *b* value and spatiotemporal parameters [Zaliapin and Ben-Zion, 2013], waveform similarity [e.g., Massa *et al.*, 2006], or spatial linkage [Dasgupta and Raftery, 1998]. We explore the clusters and examine the possibility that the

earthquakes within the cluster reflect the location of active fault segments at depth, which improves our understanding of the fault structure and tectonic regime in the DSB.

2. Tectonic Framework

More than 1100 earthquakes with magnitudes ranging from 0.5 to 5.2 were located in the DSB during 1985–2010 (Figure 2). The strongest recorded event in the last 100 years was the 1927 M_L 6.25 earthquake [Ben-Menahem *et al.*, 1976; Shapira *et al.*, 1993] (Figure 2a), whereby the mean recurrence period of $M \geq 5$ earthquakes in the DSB is estimated to be approximately 30 years [Shapira and Hofstetter, 2002]. Paleoseismologic studies demonstrate that moderate to large magnitude ($M > 7$) earthquakes have occurred in the basin area.

The DSB is approximately 150 km long and 15–20 km wide with sediments more than 10 km thick (Figure 2a). Seismic reflections and borehole data reveal that the narrow basin is bordered by steep longitudinal faults on the eastern margin, the Eastern Border Fault (EBF), and wider fault belt on its western margin, the Western Border Fault (WBF) (Figure 2). Several internal longitudinal faults are identified within the DSB including the Jericho fault (JF) [Rechtes and Hoexter, 1981], its southern continuation with the West Intrabasin Fault

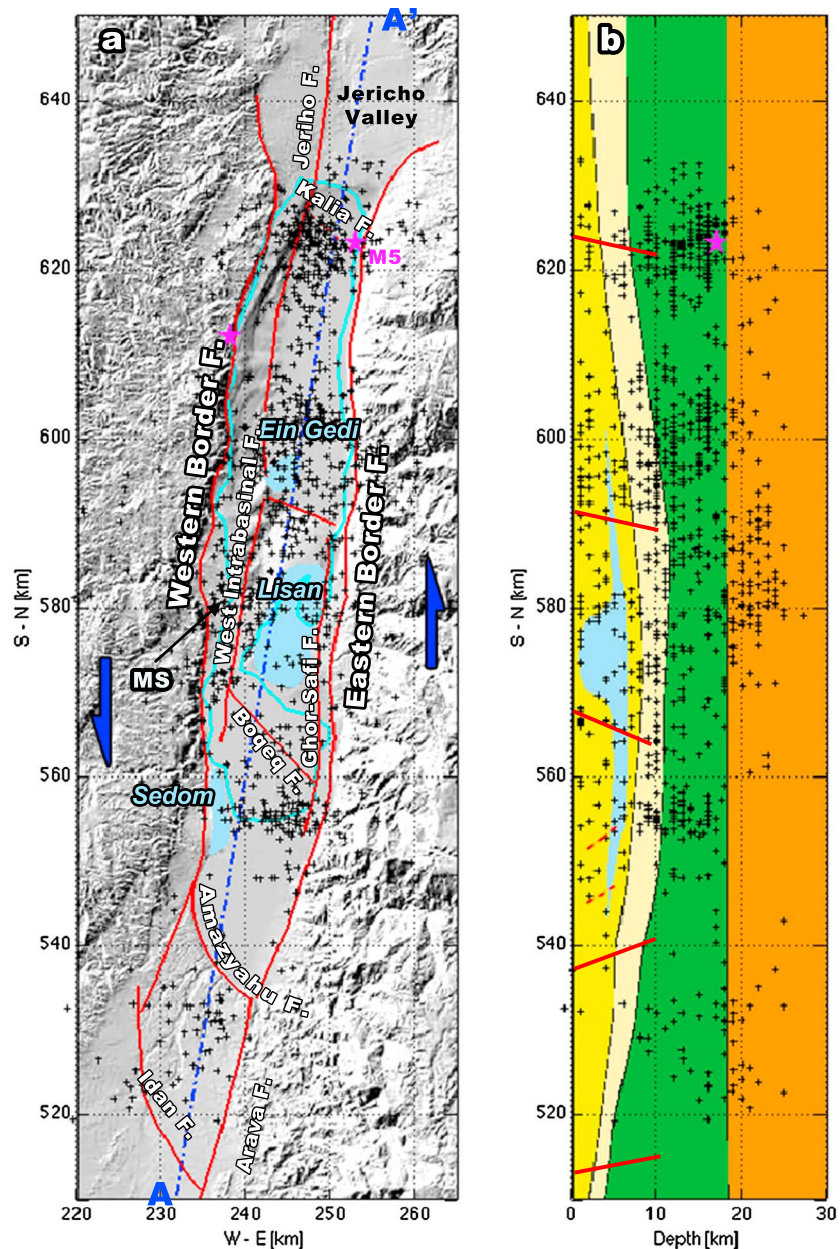


Figure 2. (a) Interpreted faults (red lines) and salt bodies (yellow polygons) in the Dead Sea basin, (modified following *Neev and Hall* [1979], *Ben-Avraham and ten Brink* [1989], and *Ben-Avraham et al.* [1993]). The black “plus” indicates the earthquake catalog (1985–2010). Stars mark the $M > 5$ magnitude earthquakes (“M5” for the 2004 event), and in cyan line, the lake shoreline; (b) projected hypocenters on a vertical S-N cross section along A-A'. Colored layers represent the structure following the seismic tomography of the DSB [*ten Brink and Flores*, 2012]: dark yellow (basin fill), light yellow (prebasin fill sediments), green (upper crust), and orange (lower crust). Red lines present the extrapolation of the faults into the crust, modified from *Ben-Avraham and Schubert* [2006]. Coordinate system is in Israel Transverse Mercator (ITM), and background Digital Terrain Model (DTM) after *Hall* [1993].

(WIF) [*Ben-Avraham et al.*, 1993], and the Ghor-Safi fault at the east [*Al-Zoubi et al.*, 2002] (Figure 2). Evidence of an ongoing N-S activity of longitudinal faults in this region is exposed in the Mor structure (“MS” in Figure 2) [*Bartov and Sagy*, 2004].

A tectonic model combining longitudinal and transverse faults was suggested by *Arbenz* [1984]. The model predicts that the accumulation of the lateral basin extension is sustained by a set of transverse faults, which merge into a midcrustal detachment zone. Although the deep seismicity along the basin rules out the

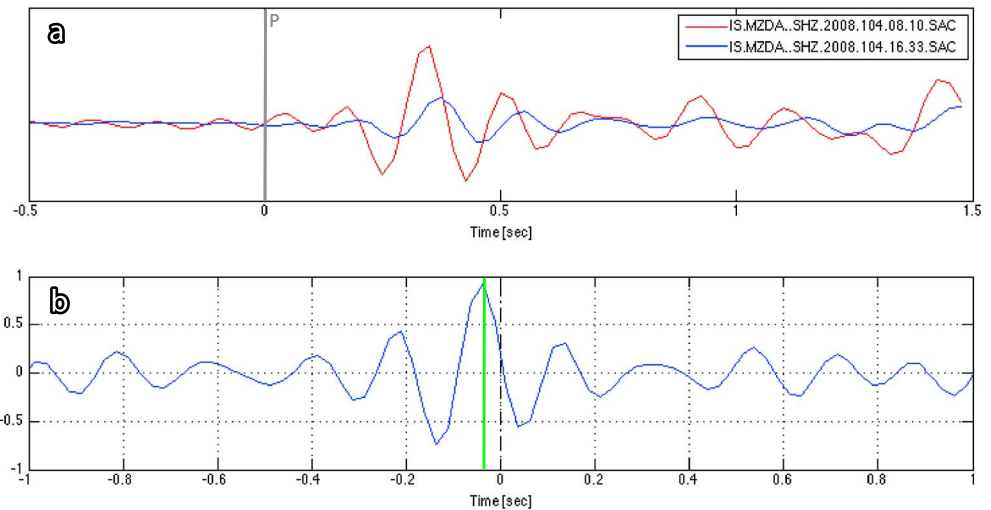


Figure 3. (a) An example for cross-correlation between two $M2$ earthquakes recorded at station MZDA in the DSB. The waveforms are shown in blue and red, and the P wave picks marked by the grey vertical line, are located at 0 s. (b) The cross-correlation between the two events (blue) and a lag time of 0.025 s between the events (green); the corresponding correlation coefficient of this pair is 0.92.

possibility of such a detachment zone, or alternatively restrict it to a ~ 5 km corridor between the Moho at ~ 30 km and the deepest seismicity at ~ 25 , several studies based on seismic reflections indicate a secondary, E-W trending fault system [Neev and Hall, 1979; Ben-Avraham and ten Brink, 1989; Larsen et al., 2002; Lazar et al., 2006; Ginzburg et al., 2007]. These faults (Figure 2a) include the Kalia fault, Ein Gedi fault, Boqeq fault, and the southern Amazyahu fault segment with a relatively vertical throw of more than 10 km [Ben-Avraham and Schubert, 2006]. In addition, several north dipping faults, ~ 10 – 15 km north of the Amazyahu fault, have been proposed by Ginzburg et al. [2007] (see dashed lines in Figure 2b).

A few salt diapirs were identified within the basin [Neev and Hall, 1979; Al-Zoubi and ten Brink, 2001; Larsen et al., 2002]. The largest one is the Lisan diapir (Figure 2a) that occupies a vast section of the central DSB and is bordered by normal faults: the WIF to the west and the Ghor-Safi fault to the east. North of the Lisan diapir, the basin is shallower with a basement depth ranging from ~ 8 km near the Lisan diapir to ~ 6 km at the present northern shore of the lake. The Sedom diapir in the southwest end of the basin (Figure 2a), which has been rising at a rate of ~ 5 mm/yr over the past 14 kyr, forms Mount Sedom [Weinberger et al., 2006], positioned above a set of east stepping normal faults with a continuation to the WIF [Larsen et al., 2002; Gardosh et al., 1997]. It was also suggested that additional shallow bodies of evaporites exist in the northern part of the basin [Ginzburg and Ben-Avraham, 1997] and that E-W trending transverse faults might be located near the present northern border of the lake and even farther north [Lazar et al., 2006].

3. Description of Data

In this study we relocate seismicity from 1985 to 2010 (about one seismic cycle [Shapira and Hofstetter, 2002]), which includes ~ 1100 events in the magnitude range of $0.5 \leq M_d \leq 5.2$, collected by the Geophysical Institute of Israel (GII), within the following geographical boundaries: 30.8°N – 31.8°N , 35.3°E – 35.65°E . The GII has been monitoring the seismic activity in the region during the past 25 years by the Israeli Seismic Network (ISN, Figure 1) consisting of a total of ~ 150 vertical seismic station components. During these years many of these stations were deactivated, and some still operate with the addition, as of 2004, of eight, three component, broadband stations. Since the ISN includes various types of seismometers, the sampling rates in the seismic station vary between 20 sps for the older stations to 50 sps for the modern ones. Several stations of the Jordanian Seismological Observatory (JSO, Figure 1) network were synched with the ISN during the time window of this work. Unfortunately, this was possible only for very short time periods, and less than 7% of the data is represented by the JSO stations.

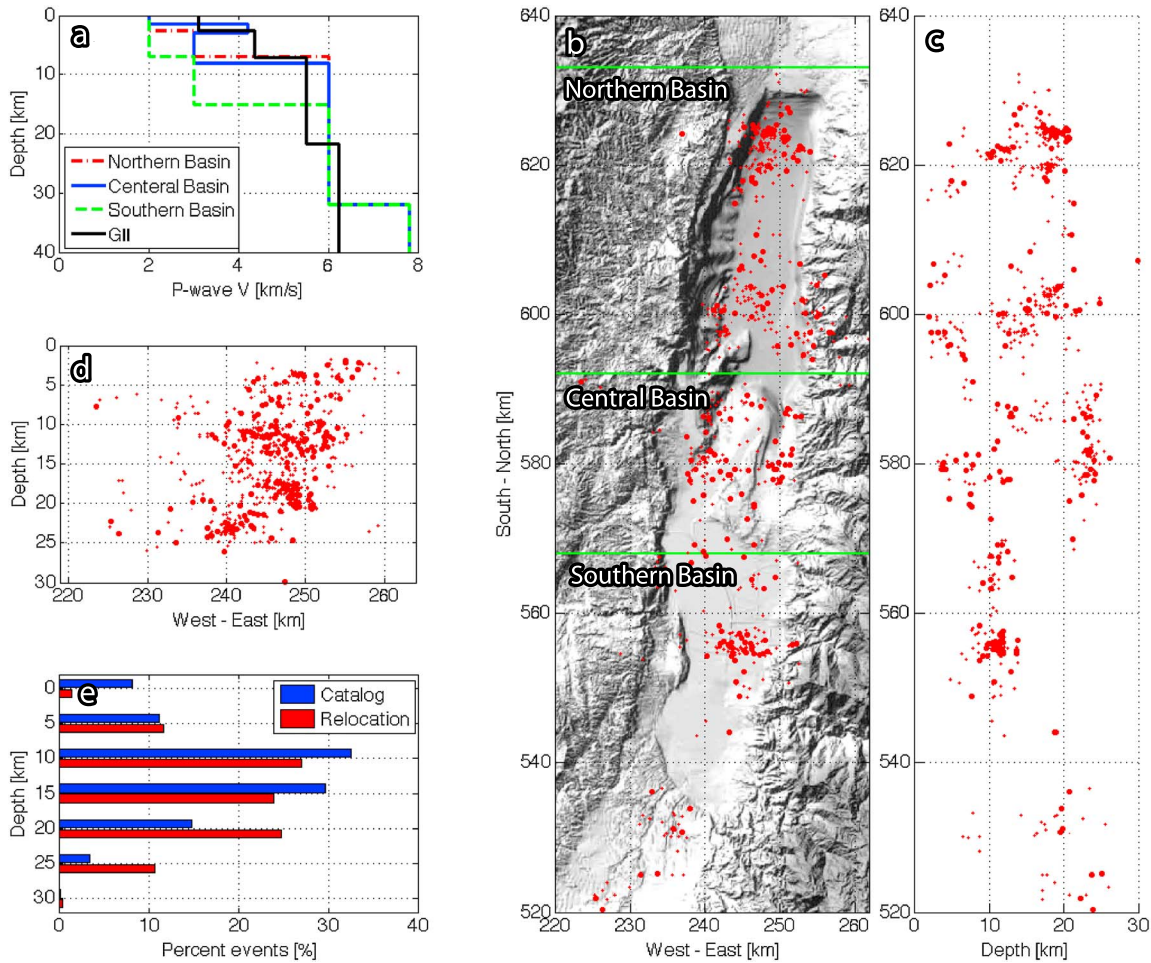


Figure 4. Relocation results. (a) *P* wave velocity models that were previously applied to the basin (GII black) and present local relocation (local velocity model, colored). Velocity models of the northern and central basins are based on a deep seismic refraction study of the DSB by Ginzburg and Ben-Avraham [1997]. The southern velocity model is a compilation of several studies [Ben-Avraham and Schubert, 2006; Mechie et al., 2009]. (b) Map and (c) North-South cross-section of the 640 relocated events. The green lines divide the regions according to the velocity models. (d) East-west cross section of the relocated catalog and (e) earthquake distribution in depth, before (catalog, blue) and after relocation (relocation, red). Coordinate system is in ITM, and background DTM is after Hall [1993].

The original catalog locations were determined by the GII, applying a 1-D velocity model (Figure 4a) and manually picking arrivals, using JSTAR software provided by the GII. The association of earthquakes with the mapped faults located by the GII (Figure 2a) is ambiguous. This may be explained by (a) errors in the location process resulting from the low resolution of the 1-D velocity model (Figure 4a, GII), (b) bias due to the one-sided seismic network located mostly on the western side of the basin (Figure 2b), and (c) significant variation in velocities, originating in the unknown internal structure and the sharp lithological variations, i.e., salt bodies forming large velocity anomalies which deflect the paths of the seismic rays.

Our analysis includes three steps: (1) relocation of the seismic events based on local velocity models, waveform cross-correlation, and catalog time differences between pairs of approximately collocated events, (2) geostatistical analysis of the relocated events, and (3) grouping the events into distinct clusters and associating the clusters with fault segments at depth and with fault traces at the surface.

4. Analytical Methods

4.1. Relocation of Earthquakes

In order to improve the earthquake locations we utilize the double-difference (DD) method, hypoDD, of Waldhauser and Ellsworth [2000]. This method has been used in many seismological studies of fault structures

and has been proven to successfully improve the locations of earthquakes. We apply two sets of differential travel times for the relocation algorithm: (1) the catalog times of *P* and *S* waves and (2) the differential times obtained from all possible waveform cross-correlation (CC) of event pairs. CC delay times have been shown to increase the accuracy of the first picks by an order of magnitude. Additionally, CC coefficients can be used to weight the data during inversion. The CC functions for the *P* waves (Figure 3) were computed using a 1.5 s window around the *P* arrivals, with time shifts of up to ± 1.5 s (following Shearer *et al.* [2003]). The waveform CC technique requires identical sample rates of the seismograms. Since the ISN operates at several different sampling rates, we resampled the waveforms to the higher sample rate before calculating the CC. In addition, we used a band-pass filter between 1 Hz and 30 Hz in order to achieve more reliable CC measurements [Hauksson and Shearer, 2005]. We cross-correlated $\sim 190,000$ event pairs with a maximum distance of 3000 m between events. Figure 3 plots an example of a high correlation between two events that were recorded at the same station.

Previous studies show that the velocity structure of the DSB changes dramatically from south to north [Ginzburg and Ben-Avraham, 1997; Ben-Avraham and Schubert, 2006; ten Brink and Flores, 2012]. Therefore, the DSB was divided into three subzones, and a 1-D local velocity model is built for each zone (Figures 4a and 4b). The velocity models are mostly derived from a deep seismic refraction [Ginzburg and Ben-Avraham, 1997] and the combination of a density-to-velocity equation [after Gardner *et al.*, 1974] that was calculated for the southern basin, using the density profile suggested by Ben-Avraham and Schubert [2006] for the lower crust and the velocity profile that is suggested by Mechie *et al.* [2009] for the upper. To include the Lisan salt diapir within the velocity model of the central basin, a decreased *P* wave velocity was placed between 3 and 8 km. The division to three subzones is the basis of our earthquake cluster analysis in the basin (section 5.1). We apply the least squares method for the relocation analysis in the hypoDD, weighting the first 10 iterations by catalog data and the later iterations weighted by the CC data.

4.2. Relocation Results

Results of the relocation are shown in map view (Figure 4b) and in S-N (Figure 4c) and W-E (Figure 4d) cross sections. The 640 relocated earthquakes show that the seismicity in the DSB has a maximum depth of ~ 25 km, as previously shown by Hofstetter *et al.* [2012], and a few kilometers less than the previous estimation of 32 km, by Aldersons *et al.* [2003], with peak activities at 12 and 17 km (Figure 4e). Figure 4e displays the depth distribution before and after the relocation. The relocated catalog shows that about 75% of the relocated earthquakes occur below 10 km and about 45% occur below 15 km. This observation correlates with the relatively low heat flux (< 40 mW/m²) measurements along the DSB [Shalev *et al.*, 2007; Shalev *et al.*, 2013] that indicate a cold and brittle crust, showing seismic activity that almost reaches the Moho at about 30 to 32 km [Ginzburg *et al.*, 1979; ten Brink *et al.*, 2006].

The relocated earthquakes show a focused view of the seismicity in the DSB (Figure 4b), compared to the corresponding, more scattered, original locations (Figure 2). In the new locations, the seismicity collapses into more discrete zones within the basin, while others became more spread out. The events are located along the eastern and western boundaries of the basin, showing patterns that roughly follow the areas of increased strain, associated with the left step-over pull-apart basin (see also Figure 5). We also note that more events are positioned along the western boundary of the basin, compared to the eastern boundary.

As previously noted, only a small part of the data are represented by seismic stations on the eastern side of the research area, resulting in uneven station coverage. However, the influence of the JSO station on the relocation is found to be relatively minor. Further details are given in the supporting information.

4.3. Geostatistical Analysis

We conducted a robust spatial analysis addressing the first-order distribution of the events with respect to the longitudinal boundary faults. The boundary faults are represented by two parallel vertical planes, spaced 9 km apart (Figure 5), striking 7°. The eastern fault trace (blue line in Figure 5) is drawn along and almost parallel to the WBF, and the west fault trace is a continuation of the JF (Figure 2) into the basin, along the WIF, and extends south to the Amazyahu fault (red line in Figure 5). The horizontal distances between the relocated epicenters and the two fault planes are calculated for six lower cutoff magnitude thresholds of 0.5, 1.0, 1.5, 2.0, 2.5, and 3, filtering out all events that are below the threshold magnitude. Maps of the filtered events, including the number of events and their percentage of the total relocated catalog, are presented in Figures 5a1 to 5a6. Events are associated with a maximum distance of 0–3 km from the planes (Figures 5b1–5b6).

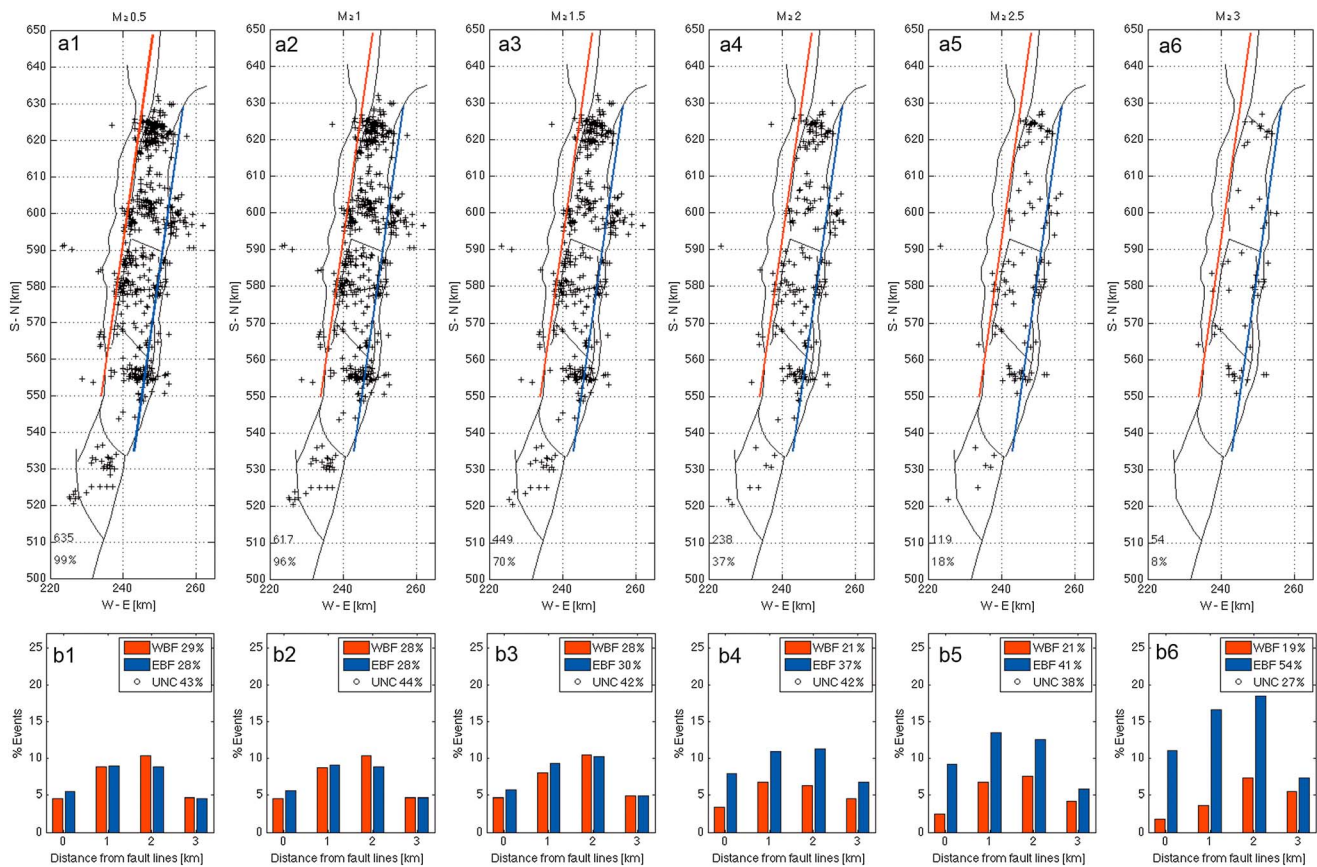


Figure 5. Seismic activity along the longitudinal faults. (a) The events are plotted (black dots) along with the mapped faults (black lines) with an exceeding magnitude threshold (shown at the top of each map). The number of the filtered events is presented at the bottom left corner along with the percentage of the unfiltered events from the total relocated catalog. The longitudinal faults are converted to two parallel lines 9 km apart. The red line represents the continuation of the JF southwest into the basin, and the blue line represents the EBF. (b) Histograms presenting the percentage of the filtered events (shown in the above image) that can be associated with the longitudinal faults, defined by a maximum of 3 km event-to-fault distance. In the legend, at the upper right corner of each histogram, is the total percentage of the associated events in the WBF (red), the EBF (blue), and the unassociated events (UNC).

The magnitude-threshold plots (Figures 5a1–5a6) demonstrate that in first order, as the magnitude cutoff threshold increases, more events can be associated with the longitudinal faults. This is manifested by the decreasing uncorrelated events (see legends of Figures 5b). The geostatistic analysis also highlights the localization of seismicity along the basin. For example, the northern tip of the basin, at $Y = 555$, shows activity for all magnitude ranges. But when moving north in the basin along the longitudinal faults, the activity decreases and fades out. Relatively inactive segments are also present within the basin. South of the northern cluster (at about $Y = 620$ in Figure 5), the seismicity is muted for 10 km to the south and appears again at $Y = 610$ (Figure 5). In the other parts of the basin (from $560 < Y < 610$) the seismicity is distributed throughout the DSB between the WBF and the EBF.

We find that the relocated catalog shows a magnitude-sensitive asymmetric seismicity that is probably an artifact originating in the lack of station coverage to the east of the DSB. Up to $M_L \sim 1.5$ (Figure 5b3) more events can be associated with the western boundary, whereas from $M_L > 2.0$ (Figure 5b4) more events can be associated with the eastern boundary. This asymmetric distribution persists at higher magnitudes, up to M_L cutoff 4, but is not presented due to the small number and percentage of the filtered events and the lack of activity at several distances. In general, the asymmetry between associated events and the WBF/EBF planes is relatively small and does not exceed $\pm 5\%$ for the discreet distances and $\sim 10\%$ for the magnitude range (Figure 5a). It is possible that there is a better detection of $M_L < 2.0$ events on the western side, closer to the network. Moreover, the fact that the number of events along the eastern boundary is higher for the $M_L > 2$ range sets a threshold of $1.5 < M_L < 2.0$ for further statistical analysis.

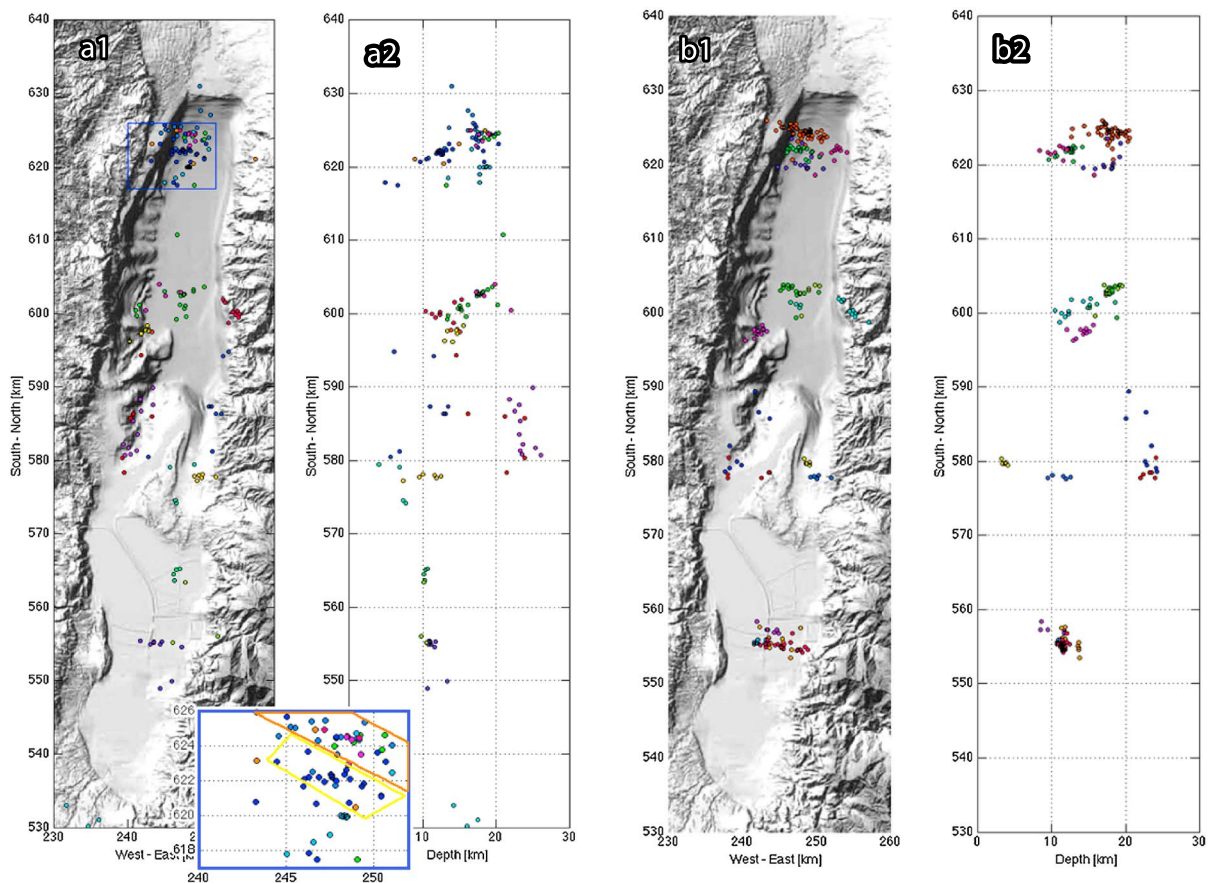


Figure 6. Clusters of earthquakes in the DSB from 1985 to 2010. The clusters are defined by two different methods: (a) waveform-based linkage with CC coefficient > 0.75 and maximum distance of 5000 m between events. The CC clustering shows a total of 167 events that are linked to 22 clusters (represented by the different colors), presented in map view (a1), and an S-N cross-section (a2); (b) Spatial and temporal clustering using a time window of 90 days and 2000 m. The ST clustering shows a total of 202 events that are linked to 18 clusters, presented in map view (b1) and S-N cross section (b2). The northern CC clusters are enlarged for convenience and the events of the M_5 aftershock is marked by the orange polygon. The cluster that is bounded by the yellow polygon is mostly composed by events of C03; Clusters C07, C08, C09, and C10 are bounded by the polygon in Figure 6b1. Coordinate system is in ITM, and background DTM after Hall [1993].

To conclude this analysis, we find that the relocated events are biased in terms of threshold detection, showing more events along the western border of the DSB up to $M \sim 2$. However, the effect on the tectonic interpretation is minor, showing clear localization along the WBF and EBF, which border the basin. Seismic activity is increased to the north and south of the basin, while other interstitial regions remain seismically inactive. This observation suggests a clear earthquake-clustered “behavior” along the basin, which is the basis of our further analysis.

4.4. Earthquake Clusters

We use two methods for identifying earthquake clusters: (1) waveform resemblance (CC clusters, Figure 6a) and (2) proximity in space and time (ST clusters, Figure 6b). The clustering algorithm used in the spatial and temporal method, also known as a hierarchical clustering method, is based on the idea of objects being more related to nearby objects than to objects farther away [Johnson, 1967]. For the ST clustering method, earthquake clusters were linked applying a time window of 90 days and a hypocenter distance of 2000 m between events (Figures 6b1 and 6b2). A total of 202 earthquakes were recognized under these criteria, forming 18 clusters with 5 to 49 events (Table 1).

As previously mentioned, it is assumed that nearby earthquakes with similar waveforms are more likely to originate from the same fault because of the similarity in the raypaths, stress field, fault geometry, and source mechanism [Baisch et al., 2008]. When the waveforms of two close events detected by the same seismic station are compared, the difference between them represents the difference between the source

Table 1. Cluster Information and Location^a

ID	X	Y	Depth	Year	Days	Events	M_{max}	nCC	CCE	Fault
C1	248.04	624.26	18	2004	210	49	5.2	8	33	JF
C2	248.00	621.80	12	2002	31	18	2.4	3	18	JF
C3	252.28	621.45	11	2007	67	10	4.3	0	0	EBF
C4	247.86	620.48	18	1989	168	11	2.4	0	0	JF
C5	246.75	602.92	19	1993	148	8	2.2	0	0	JF
C6	247.13	602.74	18	1995	2	5	2.6	2	4	JF
C7	248.79	602.67	18	2003	29	7	3.7	1	6	NS
C8	247.40	601.01	16	1999	1	5	2.4	1	4	NS
C9	254.61	600.43	12	2009	28	9	3.3	1	7	EBF
C10	242.15	597.37	14	1997	24	11	2.6	2	6	JF
C11	240.09	582.62	23	1993	205	8	4.1	0	0	WIF
C12	248.73	579.82	4	1992	3	5	3.4	1	1	GS
C13	240.61	578.56	23	1987	136	6	2.6	0	0	WIF
C14	250.23	577.89	11	2008	1	5	3.6	1	5	GS/EBF
C15	243.71	557.33	10	1986	43	6	3.2	0	0	T
C16	242.15	555.58	11	1992	1	8	3.2	1	1	T
C17	245.06	555.56	13	1987	182	11	3.7	0	0	T
C18	245.53	555.11	12	1991	110	20	3.9	1	4	T

^aThe names (ID's) are as plotted in Figures 9–11. “X,” “Y,” and “Depth” show the mean location of the cluster in the ITM coordinate system, “Days” represents the cluster time window, “Events” are the number of earthquakes in each cluster, and “ M_{max} ” is the strongest magnitude in each cluster. The number of different CC clusters that are indicated within the ST cluster is “nCC”, and “CCE” is the number of the CC cluster events that are included in a single ST cluster. The last column (“Fault”) indicate the associated fault: EBF, East Boundary Fault; JF, Jericho fault; WIF, West Intrabasinal Fault; GS, Ghor-Safi fault; NS indicates association with a NS longitudinal fault, and T is an unknown fault, suspected transverse.

parameters. Therefore, we can utilize waveform CC of earthquake couples and use the CC coefficient in order to evaluate the relation between two events, linking events with a common faulting mechanism. Hence, based on the resemblance between the waveforms, events are gathered into CC clusters, constrained by a minimum of 0.75 for the correlated coefficient, within a distance of 5 km, and recorded at a minimum of four stations (Figures 6a1 and 6a2). A total of 167 earthquakes were recognized under these criteria, forming 22 clusters of 3 to 27 events per cluster.

Figure 6 demonstrates that the two sets of relocated clusters (ST and CC) are quite similar; 91 of the events cluster in both the CC and ST clustering techniques. Therefore, the CC clusters can highlight the homogeneity of the ST clusters in terms of the source mechanism with clusters that share events using both cluster methods. The number of CC clusters that are recognized in a single ST cluster is presented in the ninth column of Table 1. Converting the magnitudes of the clustered events from local magnitudes to moment magnitudes [Shapira and Hofstetter, 2002], $\text{Log}(M_0) = (0.96 \pm 0.02) M_L + (17.59 \pm 0.05)$ suggests that about one third of the relocated catalog is linked to earthquake clusters, releasing ~68% of the total seismic moment in the basin (Table 2).

5. Association of the Clusters With the Mapped Faults

Following, we present our examination and interpretation of the cluster distribution and the possible association of the clusters (Table 1) with the previously mapped faults (Figure 2).

Table 2. Regions, Clusters, and Seismic Moment^a

Region	Events	C Events	%	Clusters	Cluster Moment	Total Moment	% Moment
Northern	335	171	51	10	5.74E + 22	6.87E + 22	83
Central	148	50	34	4	1.37E + 22	2.53E + 22	54
Southern	157	58	37	4	1.17E + 22	2.65E + 22	44
Total	640	279	43	18	8.28E + 22	1.21E + 23	68

^aEvents are the number of the relocated events in the region. “C events” are the number of events that are linked to clusters in the region.

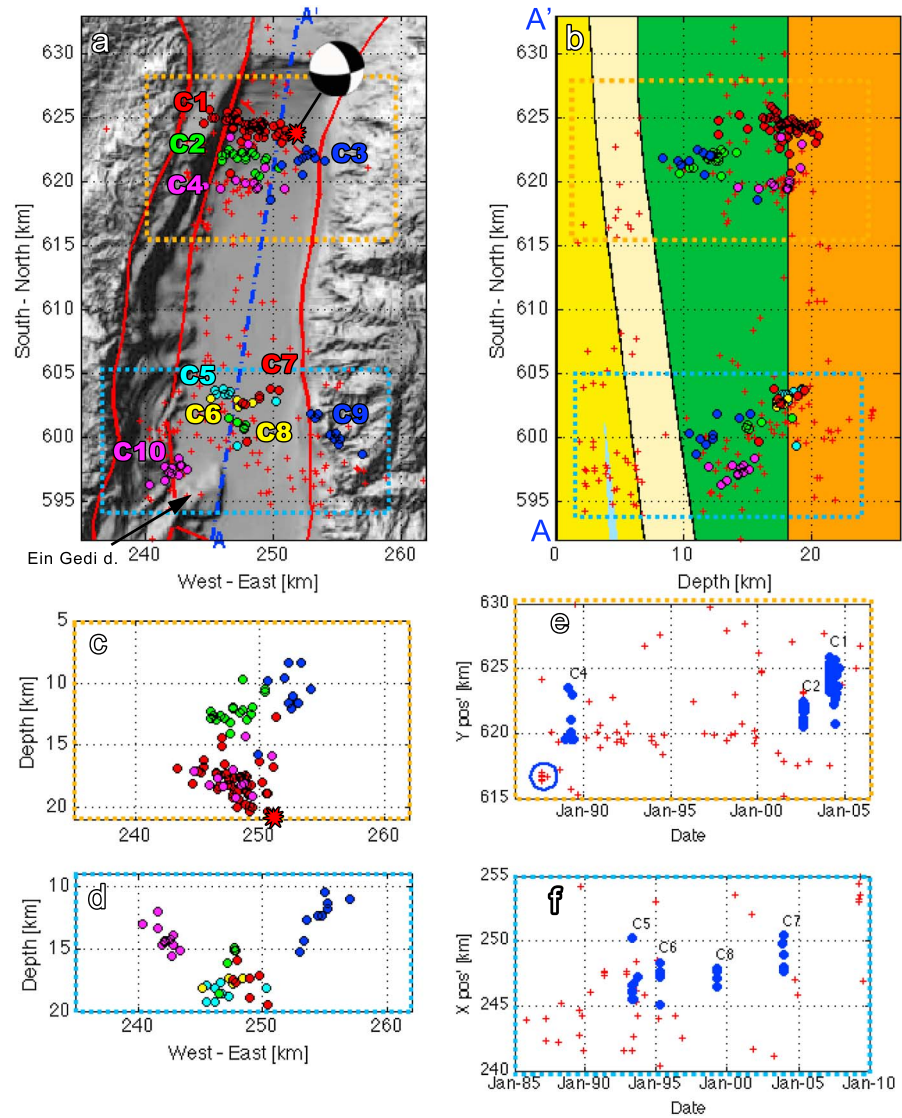


Figure 7. The northern DSB. (a) Map of the northern DSB including 10 clusters that contain 171 events; the M_5 event is shown by the red “star.” (b) South-north depth cross section of the relocated clusters along the A'-A dashed blue line. The focal mechanism of the $M_5.2$ event of 2004 is presented [Hofstetter *et al.*, 2008], and black line points to the epicenter. The cluster details are presented in Table 1. Colored layers represent the structure following the seismic tomography of the DSB [ten Brink and Flores, 2012]: dark yellow (basin fill), light yellow (prebasin fill sediments), green (upper crust), and orange (lower crust); (c and d) West-east depth cross section of the two cluster groups: northern (orange rectangle) and southern (pale blue rectangle). (e) Temporal distribution of two cluster groups showing a south to north cluster migration over time. (f) Temporal migration of the clusters eastward. Relocated earthquakes are plotted in red “plus” in all figures. Coordinate system is in ITM, and background DTM after Hall [1993].

5.1. Earthquake Clusters in the Northern DSB

A total of 335 events were relocated in the northern DSB of which 171 were linked in 10 clusters (clusters C1–C10 in Table 1). The clusters are grouped in two main regions, separated by a relatively aseismic region of 10 km (from 605 to 615, Figures 7a and 7b).

The northern group includes four ST clusters and four CC clusters trending in a W-E formation (Figure 7). The largest cluster of this catalog is the C1 cluster, with a total of 49 events, including the strongest event within the catalog, the M_L 5.2 earthquake of 11 February 2004 (M_5) (Figure 2). The aftershock sequence shows a strike of $\sim 290^\circ$ ($R^2 \sim 0.55$) and shows a subplanar seismicity dipping eastward at $\sim 45^\circ$ (red cluster, Figure 7c).

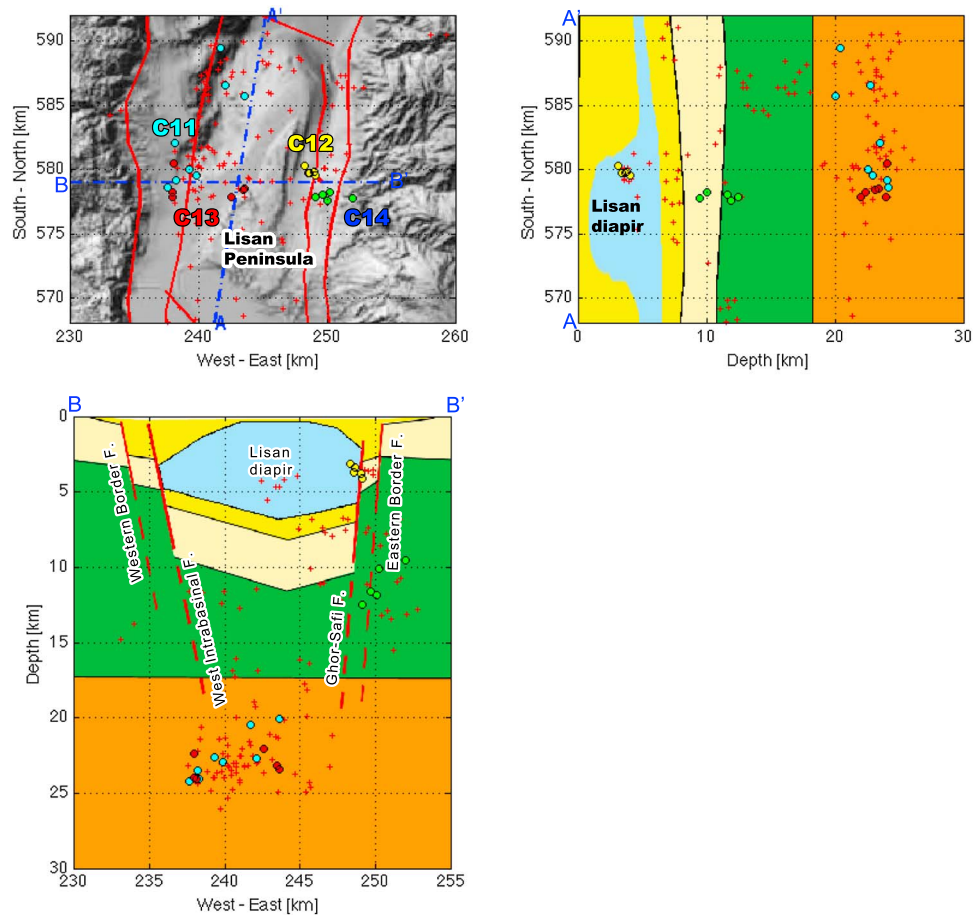


Figure 8. The central DSB. (a) Map of the central DSB including the four clusters that contain a total of 50 events. (b) South-north depth cross section (A-A') of the relocated clusters. The clusters (by number) are detailed in Table 1. Colored layers show interpreted structure following the seismic tomography of the DSB [ten Brink and Flores, 2012] and interpretation of Bouguer gravity data [Choi et al., 2011]: dark yellow (basin fill), light yellow (prebasin fill sediments), green (upper crust), orange (lower crust). (c) West-east depth cross section according to B-B', dashed line in Figure 8a. Relocated earthquakes are plotted in red plus. Background image follows Al-Zoubi and ten Brink [2001] and ten Brink and Flores [2012]. Coordinate system is in ITM, and background DTM after Hall [1993].

Directivity analysis of the *M*5 event shows that motion occurred on a N-S trending fault [Hofstetter et al., 2008] that does not align with the W-E trend of the cluster nor with the configuration of the Kalia fault that was interpreted as a south dipping transverse fault [Lazar et al., 2006]. Eight CC clusters are included within cluster C1 (Table 1). The multiple CC clusters may reflect the magnitude range (2–5.2) of the cluster, and the various types of faulting mechanisms, including normal, oblique reverse and mostly strike-slip solutions as was computed by Hofstetter et al. [2008].

Cluster C2 (Figure 7) of the northern group includes 18 events, all share a single CC cluster, almost parallel to the C1 cluster (Figure 6a) and with a 60° northward dip (Figure 6b).

Several ST clusters show a spatial migration over time. The migrated activity began on 22 July 1987 (circled in blue, Figure 7d), propagated northward (C4 and C2, Figure 7a), and ended on 15 August 2004 with cluster C1. Figure 7d presents the temporal distribution of the four clusters of the northern group. From this point (in time), the activity shifted eastward with cluster C3, positioned with the continuation of the E-W trend of cluster C1 eastward, reaching to ~200 m west of the EBF (Figure 7a).

Within the southern group, clusters C5–C8 include 25 events located at the center of the basin with an average depth of ~17 km (Figure 7a). East of this group, cluster C9 is located along the EBF at a depth range of 10–15 km and is highlighted by a single CC cluster (red, Figure 6a1). West of this group, cluster C10 is located

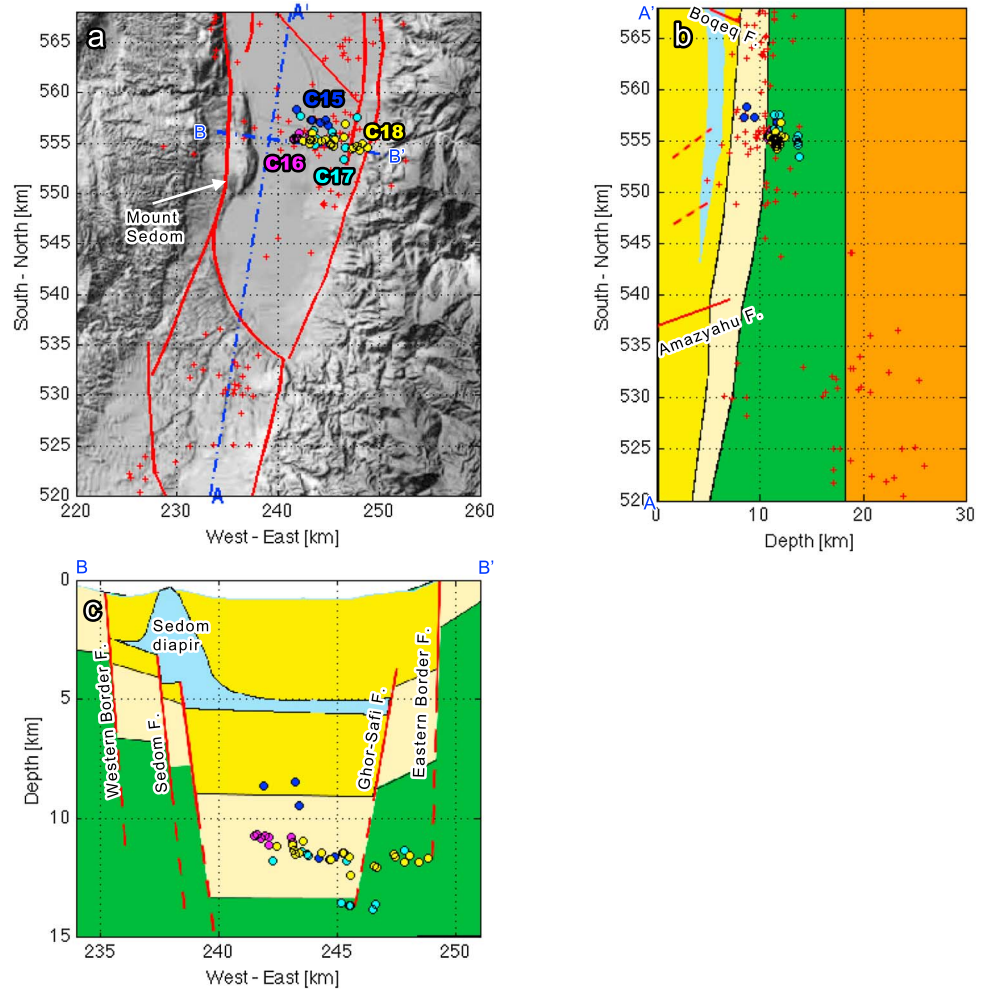


Figure 9. The southern DSB. (a) Map of the southern DSB including the four clusters that contain a total of 57 events. The clusters (by number) are detailed in Table 1. Relocated earthquakes are plotted in red plus. (b) Cross sections A-A'; colored background layers show interpreted structure following the seismic tomography of the DSB [ten Brink and Flores, 2012]: dark yellow (basin fill), light yellow (prebasin fill sediments), green (upper crust), and orange (lower crust). (c) East-west depth cross section (B-B') with a background image showing seismic interpretation following Ben-Avraham and Schubert [2006] and Al-Zoubi et al. [2002]. Coordinate system is in ITM, and background DTM after Hall [1993].

~1 km NE of the Ein Gedi salt diapir at a depth range of 12–15 km (Figure 7a). The cluster is composed of 11 events in a time window of 23 days with maximum magnitudes of 2.6. Although the cluster is in close proximity to the Ein Gedi diapir and a few kilometers below the salt layer, it is also located at a junction of the WIF [Smit et al., 2008] and the Ein Gedi fault. Therefore, it is more reasonable that this activity is associated with the WIF and not related to salt tectonics. East-west cross section (Figure 7d) shows activity at the center of the basin at a depth of ~17 km bounded by activity along the longitudinal boundary faults dipping ~60° toward the center of the basin. Figure 7f shows that this activity started with cluster C5 in 1993, propagated to the east with clusters C6 and C8, and ended in December 2003 with cluster C7 about 1.5 km west of the EBF (Figure 7a). The pattern is also highlighted by 15 of the CC cluster events of three of the clusters (C6–C8) and by a north dipping, single CC cluster (“green” at Y= 601, Figure 6a1 and 6a2), at a depth range of 12–20 km (Figure 6a2).

5.2. Earthquake Clusters in the Central DSB

Of the 148 total events relocated in the central basin, 50 are grouped into four clusters (C11–C14 in Table 1 and in Figure 8), located east (C12 and C14) and west (C11 and C13) of the Lisan Peninsula (Figure 8a).

Of the 119 events, 76 are located between $565 < Y < 590$ km (Figure 8), beneath the Lisan diapir. This activity is highlighted by clusters C11 and C13, the deepest in the basin, showing an average depth of 22 km. The clusters consist of 14 events with magnitudes ranging up to M_L 4.1. Depth cross sections (Figures 8b and 8c) show that the two deep western clusters (C11 and C13) are part of a relatively horizontal activity that extends north toward the En Gedi fault ($Y = 590$, Figure 8b). Based on the spatial distribution of these clusters, it is possible that the deep activity is associated with the WIF. Deep longitudinal activity is also highlighted by two CC clusters, shown west of the Lisan diapir with a total of 17 events located at a depth range of ~ 23 km (purple and red clusters in Figures 6a1 and 6a2). East of the Lisan diapir, the locations of two clusters (C12 and C14, Figure 8) show activity along the interpreted EBF and the Ghor-Safi fault.

We suggest that the clusters of the central DSB mainly highlight the longitudinal eastern and western boundary faults that border the Lisan salt diapir, but with no connection to salt tectonics, since most of the activity lies deep below the salt body (Figures 8b and 8c).

5.3. Earthquake Clusters in the Southern DSB

The seismicity of the southern basin includes 157 events, conjoined into four clusters (C15–C18), including a total of 45 events that form linear bands east of Mount Sedom (Figure 9) at depths of 8–12 km (Figures 9b and 9c).

As previous microseismological investigation at this site shows [Braeuer *et al.*, 2012], the EBF is active and produces seismic activity at about a 90° dip. Such activity is shown with clusters C17 and C18, located at a depth range of ~ 12 km at the bottom of the interpreted Ghor-Safi fault (Figure 9c).

While part of the activity is located at the lower EBF (Figure 9c), the clusters extend ~ 7 km west of the EBF toward the center of the lake (see cluster C18 in Figures 9a and 9c). Cluster C16 is the westernmost of this group. It consists of eight events that occurred on 26 June 1992, with magnitudes up to 3.2, at a depth range of ~ 10 km, located ~ 5 km west of the Ghor-Safi fault (Figure 9). This activity could be interpreted as several subparallel longitudinal faults that are located west of the Ghor-Safi fault. Alternatively, the extension of the seismicity toward the center of the basin may suggest that the activity is not restricted only to the eastern longitudinal faults. Another indication of a secondary fault system is demonstrated by a single CC cluster in this part of the basin (“purple” at $Y = 555$, Figure 6a), which may possibly highlight a similar source signature trending E-W.

Although the Amazyahu fault is well defined in seismic reflections down to depths of 7 km [Ginzburg *et al.*, 2007], the level of seismicity is rather low with no indication of clustering and with no seismic activity detected near the Sedom diapir.

6. Discussion

We demonstrate that between 1985 and 2010 the activity in the DSB was not randomly distributed and could be partly grouped into well-defined and possibly physically meaningful clusters. Regarding some of the clusters that appear to have a dominant E-W trend (e.g., C1 and C2 in Figure 7), we note that one-sided station distribution can produce an artificial lineation toward or away from the network, regardless of the location method used. This is because origin time can be a trade-off with distance from the network. The shift can be either toward (later origin time) or away (earlier origin time) from the network, especially if the catalog locations and origin times were used as the starting locations (in the case of hypoDD). This effect on the E-W direction is accounted for, and clusters that trend E-W are interpreted under the previous consideration.

Tempo-spatial methods were applied to link about 30% of the relocated events into 18 clusters, releasing about two thirds of the seismic moment (Table 2), reliably representing the strain distribution along the basin. About one quarter (26%) of the data is linked using the CC method. For comparison, cluster analysis of relocated events in southern California based on waveform CC and natural neighborhood show that about 10 to 30% of the events belong to clusters of similar events [Shearer *et al.*, 2003].

6.1. Activity Along Longitudinal Faults

The tectonic configuration of pull-apart basins dictates that in first order, the longitudinal faults are the main carrier of the regional plate motion. The relocation and the cluster analysis support this concept, as the eastern and western border faults are highlighted by the seismicity throughout the basin in several areas.

About 75% of the events that are included with the ST clusters are interpreted here as activity that is associated with the longitudinal faults (Table 1). The geostatistical analysis also indicates that more events can be associated with the main faults within the close range as the magnitude cutoff increases. The analysis shows a minimum recurrence of association within the first bar ("0 km") and a maximum in the second ("1 km") and the third ("2 km") ranges for almost all magnitudes (Figure 5), which can be interpreted as an expression of the faults' dip. The geostatistical analysis also reflects the possibility that the eastern boundary of the DSB is slightly more active throughout the entire basin, as previously shown only for the southern and central DSB over a time window of 17 months [Braeuer *et al.*, 2012].

The longitudinal faults are highlighted also by deep activity. About 18% of the relocated events are below 20 km, indicating a cold crust in the region of the DSB [Shalev *et al.*, 2013]. Although deeper activity is located along the western side of the basin, it is highly possible that this asymmetry is a product of biased event detection, as most of the deep activity is in the magnitude range of ~ 1.5 , the lower threshold of detection shown by the geostatistical analysis. It is also possible that the concentration of deep events along the western part of the basin indicates that the western plate is colder [Reches, 1987].

The cluster analysis in the northern part of the DSB presents two cluster groups, 10 km apart (Figure 7). The southern group is composed of six clusters that highlight the east and west longitudinal boundary faults (C9 and C10), dipping toward the center of the basin (Figure 7b). The rest of the clusters (C5–C8, Figure 7) are located in the center of the basin ~ 17 km deep. Previous geophysical works [Neev and Hall, 1979; ten Brink and Ben-Avraham, 1989; ten Brink and Flores, 2012] show no indication of a transverse fault. It is highly possible that the localization of the four clusters in the center of the basin indicate the geometrical interaction between the JF and the EBF as was recognized by a "Y"-shaped seismicity by Hofstetter *et al.* [2007] in several locations along the basin.

We conclude that the longitudinal faults are represented by the micro-earthquake activity throughout the basin and highlighted in several locations by the earthquake clusters. We also note that the spatial distribution of the earthquakes reflects the geometry of the longitudinal faults.

6.2. Strain Accumulation and Seismic Activity in the Northern Part of the Basin

Seismic reflections and palaeoseismic analysis demonstrate that north of the lake, the JF (Figure 2) is the main active strike-slip segment of the transform [Reches and Hoexter, 1981; Rotstein *et al.*, 1991; Shapira *et al.*, 1993; Lazar *et al.*, 2006]. Yet our observations show a sharp decrease of the seismicity in the Jericho valley (Figure 2), suggesting that the JF north of the lake (i.e., in the Jericho valley) is seismically locked. On the other hand, the northern DSB, south of the Jericho valley has been the most active zone in the area during the past 25 years (Figure 7). The activity consists of several micro-earthquake clusters and a main shock (the M_5 event).

We show that the directivity of the M_5 event and its aftershock cluster are not consistent with the main faults in this area (JF, EBF, and the suggested Kalia fault, Figure 2). The combination of the focal mechanism and the directivity of the M_5 event suggest an oblique left-lateral component of an eastward dipping fault (strike 343, dip 54, and rake 338), with a rather small component of reverse motion (Figure 7a).

However, experimental and theoretical predictions of faulting near the edge of a main fault in a segmented strike-slip system demonstrates that faults propagate into the regions of lower mean stress [Segall and Pollard, 1980; Reches, 1987; Katzman *et al.*, 1995; ten Brink *et al.*, 1996]. In the case of brittle pull-apart basins, the tips of the faults are predicted to propagate toward one another [Reches, 1987; Segall and Pollard, 1980]. Therefore, we interpret the M_5 earthquake as out-of-plane faulting in the edge zone of the EBF (Figure 7). We find that this conceptual model matches the structure of the main and the predicted faults (top right inset of Figure 10a). Note that on 12 September 2013, a ~ 3.5 M event with a similar focal plane solution occurred at a depth of 16 km, 7 km north (azimuth $\sim 10^\circ$) of the 2004 M_5 event. Moreover, our cluster analysis suggests propagation of the activity northward, as well as an overall deepening (Figures 6b2 and 7d). Such activity might express propagation of deformation and strain accumulation prior to the M_5 event. Similar progressive sequences of earthquakes prior to a relatively large earthquake were documented in strike-slip faults [Stein *et al.*, 1997], subduction zones [Lin and Stein, 2004], and simulated by laboratory experiments [Rubinstein *et al.*, 2011].

The aftershock sequence that followed the M_5 event trends in an E-W linear band. We suggest that this orientation is an effect of static stress changes, promoting the earthquake failure [e.g., Stein, 1999]. Figure 10

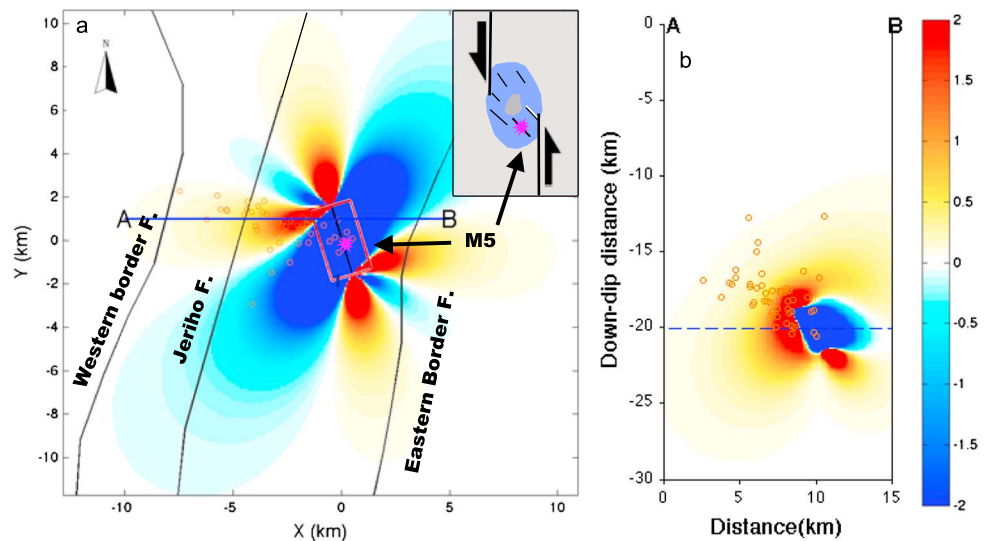


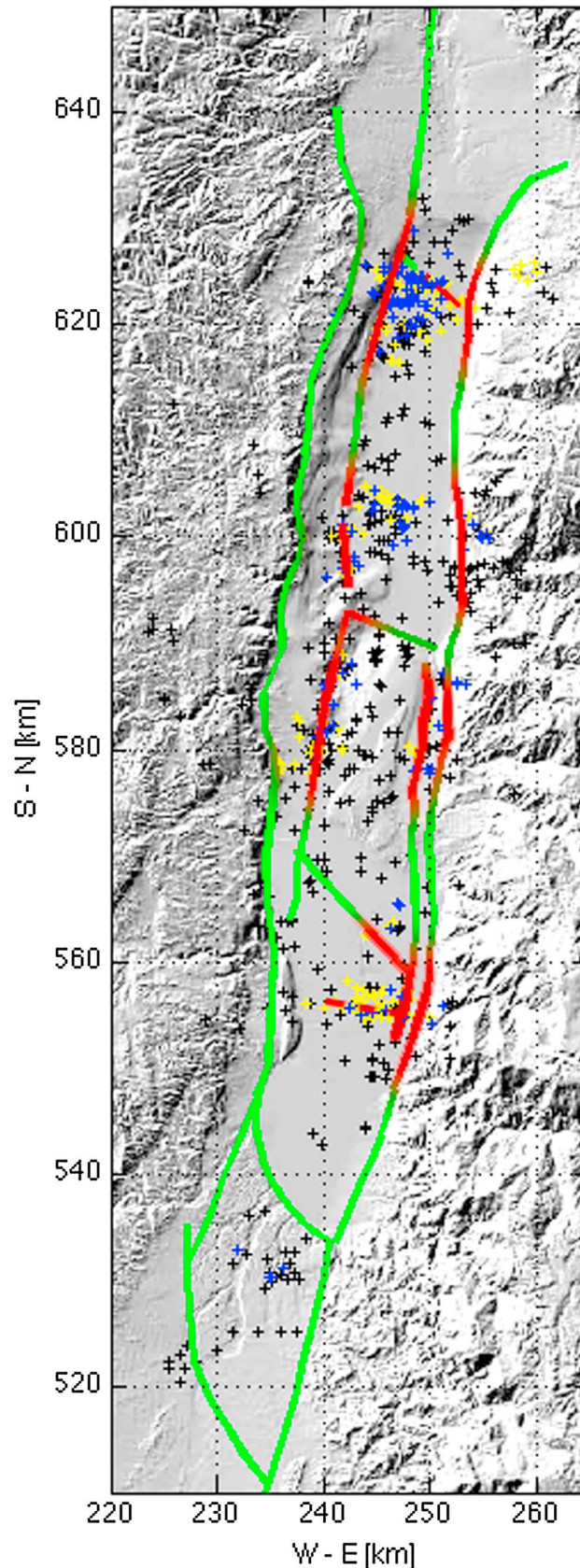
Figure 10. Coulomb stress zone at (a) depth of 20 km, and (b) along the cross section A-B. The main shock is marked by the black arrow (*M5*), aftershocks (orange circles), mapped faults at the surface, and the color bar represents the rupture area stress changes, measured in bars. A predicted structure of a pull apart in brittle material is shown in Figure 10a at the upper right corner [after *Reches, 1987*]. Light blue area marks a subsidence area, and the ticked lines mark the predicted faults.

illustrates the correspondence of the C2 aftershocks (red circles) with the increased Coulomb stress changes (red regions) in a map view (Figure 10a) and in a NE-SW cross section (Figure 10b). The main shock source parameters that are used as input for the Coulomb 3.3 software to calculate Coulomb stress change [Lin and Stein, 2004; Toda *et al.*, 2005] are as calculated by Hofstetter *et al.* [2008] for the *M5* event. The input friction is 0.6, and the rupture length is calculated using empirical relations following Wells and Coppersmith [1994].

We suggest that ongoing strain accumulation northward precedes the *M5* event on a secondary fault. Our analysis shows that the aftershock sequence that accompanied the *M5* event aligns with the increased calculated Coulomb stress change and might reflect triggering of another secondary fault. Furthermore, the increased seismicity, the multiple source mechanisms, and the geometrical shape of the clusters indicate seismic activity on several segments, some of them unmapped, suggesting that this part of the basin is relatively young. We assume that a continuation of this stress accumulation will eventually lead to rupture along the locked section of the JF north to the present lakeshores.

6.3. Activity Along Transverse Faults

Our analysis, as discussed above, suggests that the majority of the activity along the DSB is associated with the N-S bounding faults. However, several clusters in the southern part of the DSB (e.g., C15–C18) are characterized by a spatial distribution that cannot be explained by the N-S longitudinal faults. These clusters are localized at depth, trending WNW-ESE, and extend from the EBF toward the center of the basin (Figure 9a), although the longitudinal eastern faults, the EBF and the Ghor-Safi fault, appear vertical in seismic reflection surveys [Arbenz, 1984; Al-Zoubi *et al.*, 2002] and are supported by microseismic activity [Brauer *et al.*, 2012]. Therefore, we examine the possibility of associating the southern activity to a transverse faulting. The closest indication of a transverse fault to the cluster bands is the Boqeq fault (Figure 2), interpreted as a south dipping normal fault [Ben-Avraham and Schubert, 2006]. While at the surface the fault is ~5 km north of the cluster epicenters, it is possible that at a depth of ~10 km the Boqeq fault intersects the hypocenters. However, since the clusters lie a few kilometers below detection of the available seismic reflection data, and with no direct indication of the style of the faulting (i.e., focal mechanism analysis), the association of these clusters with the Boqeq fault remains speculative. It is also possible that this activity is associated with an unmapped, relatively small, E-W trending fault, similar to the faults that are identified in the southern DSB between the Amazyahu and the Boqeq faults (see dashed red lines in Figure 2b and Figure 9b following Ginzburg *et al.* [2007]). If such a fault exists, we could expect a localized earthquake distribution on a map across the basin (clusters C15–C18).



6.4. The Active and the Quiescent Fault Segments in the Basin

Our analysis suggests that many of the clusters along the DSB can be associated with the N-S bounding faults. On the other hand, the southern transverse Amazyahu fault segment (Figure 9), which is clearly visible at the surface, and in geophysical interpretation [Ginzburg et al., 2007], did not generate cluster seismicity within the time window of the research. It is possible that the Amazyahu fault is locked in the time period of this research.

We find that other fault segments are seismically silent within the time window of the research, including the JF north of the lake. We assume that the seismic quiescence reflects that the fault was locked in the northern part of the basin because it is clear that it was previously activated by large historical earthquakes [Reches and Hoexter, 1981; Lazar et al., 2010].

7. Conclusions

Earthquake relocation and two different methods for defining earthquake clusters have been used to detect and characterize the seismic activity in the DSB. While the original earthquake catalog may look chaotic at first sight, relocation analysis shows that earthquake collapses to certain more discrete zones along the basin, while others become more spaced (Figure 4), reflecting activity of specific fault segments in the basin. About one third

Figure 11. Cluster-associated fault map. The fault sections associated with microseismicity are marked by the red lines, while the quiescent fault segments are marked in green. Relocated earthquakes are plotted by black plus, earthquakes that are linked to ST clusters are marked by yellow plus, and CC clusters are shown in blue plus. The faults presented were previously interpreted, mostly by seismic reflection surveys [Neev and Hall, 1979; Ben-Avraham and ten Brink, 1989; Ben-Avraham et al., 1993]. Coordinate system is in WGS84, and background DTM after Hall [1993].

of the data is linked to 18 earthquake clusters using spatiotemporal criteria (ST clusters, Figure 6b), and about one quarter is linked to clusters based on waveform resemblance (CC clusters, Figure 6a). The total clustered activity includes a total of 279 events that represent the majority of the released seismic energy in the basin (Table 2).

About 75% of the microseismic activity that is linked to the ST clusters is associated with N-S trending faults. The EBF and JF and its continuation southward are highlighted by cluster activity in the north (Figure 7) and by the deep activity east and west of the Lisan Peninsula (Figure 8). The geostatistical analysis supports the cluster interpretation, showing that earthquakes in the DSB are mostly associated with the main longitudinal faults (Figure 5) and is therefore consistent with the pull-apart model, which suggests increasing activity along longitudinal faults.

We find evidence of a predominant transverse fault in the southern part of the DSB, suggesting an association with the Boqeq fault or alternatively, with another secondary ~E-W trending fault that was mapped north of the Amazyahu fault (dashed red line, Figure 11).

The occurrence of the clusters and their distribution in the northern DSB indicates progression of the activity northward, probably along the JF (Figure 7). The northward propagation may relate to the accumulated left-lateral motion of the DST (Figure 1) and the global northward motion of the Arabian Plate. The *M*₅ earthquake is explained here as a secondary fault at the tip of the EBF, and the aftershock sequence that followed the *M*₅ event corresponds to the local increase of Coulomb stress. We also note that the varied CC clusters identified within the *M*₅ aftershock sequence support the multiple types of focal mechanisms that were previously calculated [Hofstetter *et al.*, 2008]. Therefore, we interpret this cluster as relatively recent, suggesting that the northern basin is relatively young.

The compilation of our seismological analyses in the entire basin (Figure 11) shows the “activeness” of major mapped faults within the time period of the past 25 years. We show that while the seismic activity is associated with several faults along the basin, some faults remain quiescent throughout the entire time window of this study (e.g., Amazyahu fault). Overall, our analysis is in agreement with the general fault geometry of the DSB, suggesting two main boundary faults and transverse faults between them [Zak *et al.*, 1981; ten Brink and Ben-Avraham, 1989]. We note that in order to achieve better constraint of the faults-to-cluster association, a 3-D velocity model should be applied with the location/relocation, e.g., NonLinLoc (<http://alomax.free.fr/nlloc/>). Such a method can overcome the variations of the velocity model, within and outside the basin, and clarify the uncertainty regarding the E-W trend of several clusters.

Acknowledgments

We thank the two anonymous reviewers and Robert Nowack (Editor) for thoughtful and helpful comments and suggestions. We thank Ze'ev Reches and Ittai Kurzon for their critical reviews and insights that greatly improved the paper. We also thank Rami Hofstetter and Batia Baruch for providing us the seismic data and technical support with the location software. This research was supported by The Israel Science Foundation (grant 1736/11 to SM).

References

- Aldersons, F., Z. Ben-Avraham, A. Hofstetter, E. Kissling, and T. Al-Yazjeen (2003), Lower-crustal strength under the Dead Sea basin from local earthquake data and rheological modeling, *Earth Planet. Sci. Lett.*, *214*(1–2), 129–142, doi:10.1016/s0012-821x(03)00381-9.
- Al-Zoubi, A. S., and U. S. ten Brink (2001), Salt diapirs in the Dead Sea basin and their relationship to Quaternary extensional tectonics, *Mar. Pet. Geol.*, *18*(7), 779–797, doi:10.1016/S0264-8172(01)00031-9.
- Al-Zoubi, A. S., H. Shulman, and Z. Ben-Avraham (2002), Seismic reflection profiles across the southern Dead Sea basin, *Tectonophysics*, *346*(1–2), 61–69.
- Arbenz, J. K. (1984), Oil potential of the Dead Sea area. *Rep. 84/111*, 54 p., Seismica Oil Exploration Ltd., Tel Aviv, Israel.
- Baisch, S., L. Ceranna, and H.-P. Harjes (2008), Earthquake cluster: What can we learn from waveform similarity?, *Bull. Seismol. Soc. Am.*, *98*(6), 2806–2814, doi:10.1785/0120080018.
- Bartov, Y., and A. Sagy (2004), Late Pleistocene extension and strike-slip in the Dead Sea Basin, *Geol. Mag.*, *141*(5), 565–572, doi:10.1017/S001675680400963X.
- Ben-Avraham, Z., and G. Schubert (2006), Deep “drop down” basin in the southern Dead Sea, *Earth Planet. Sci. Lett.*, *251*(3–4), 254–263.
- Ben-Avraham, Z., and U. S. ten Brink (1989), Transverse faults and segmentation of basins within the Dead Sea Rift, *J. Afr. Earth Sci.*, *8*(2–4), 603–616, doi:10.1016/s0899-5362(89)80047-8.
- Ben-Avraham, Z., T. M. Niemi, D. Neev, J. K. Hall, and Y. Levy (1993), Distribution of Holocene sediments and neotectonics in the deep north basin of the Dead Sea, *Mar. Geol.*, *113*(3–4), 219–231.
- Ben-Menahem, A., A. Nur, and M. Vered (1976), Tectonics, seismicity and structure of the Afro-Eurasian junction—The breaking of an incoherent plate, *Phys. Earth Planet. Inter.*, *12*(1), 1–50, doi:10.1016/0031-9201(76)90005-4.
- Brauer, B., G. Asch, R. Hofstetter, C. Haberland, D. Jaser, R. El-Kelani, and M. Weber (2012), Microseismicity distribution in the southern Dead Sea basin and its implications on the structure of the basin, *Geophys. J. Int.*, *188*(3), 873–878.
- Chiaraluce, L., W. L. Ellsworth, C. Chiarabba, and M. Cocco (2003), Imaging the complexity of an active normal fault system: The 1997 Colfiorito (central Italy) case study, *J. Geophys. Res.*, *108*(B6), 2294, doi:10.1029/2002JB002166.
- Choi, S., H.-J. Götze, U. Meyer, and D. Group (2011), 3-D density modelling of underground structures and spatial distribution of salt diapirism in the Dead Sea Basin, *Geophys. J. Int.*, *184*(3), 1131–1146.
- Dasgupta, A., and A. E. Raftery (1998), Detecting features in spatial point processes with clutter via model-based clustering, *J. Am. Stat. Assoc.*, *93*(441), 294–302, doi:10.2307/2669625.

- Fukuyama, E., W. L. Ellsworth, F. Waldhauser, and A. Kubo (2003), Detailed fault structure of the 2000 western Tottori, Japan, earthquake sequence, *Bull. Seismol. Soc. Am.*, *93*(4), 1468–1478, doi:10.1785/0120020123.
- Gardner, G. H. F., L. W. Gardner, and A. R. Gregory (1974), Formation velocity and density—The diagnostic basics for the stratigraphic traps, *Geophysics*, *39*(6), 770–780.
- Gardosh, M., E. Kashai, S. Sallhov, H. Shulman, and E. Tannenbaum (1997), Hydrocarbon exploration in the southern Dead Sea area, in *The Dead Sea, the Lake and Its Setting*, edited by T. M. Niemi, Z. Ben-Avraham, and J. P. Gat, pp. 57–72, Oxford Univ. Press, New York.
- Garfunkel, Z. (1981), Internal structure of the Dead Sea leaky transform (rift) in relation to plate kinematics, *Tectonophysics*, *80*(1–4), 81–108.
- Garfunkel, Z. (1997), The history and formation of the Dead Sea basin, in *The Dead Sea, the Lake and Its Setting*, edited by T. M. Niemi, Z. Ben-Avraham, and J. R. Gat, pp. 36–56, Oxford Monographs on Geology and Geophysics, New York.
- Garfunkel, Z., and Z. Ben-Avraham (1996), The structure of the Dead Sea basin, *Tectonophysics*, *266*(1–4), 155–176.
- Garfunkel, Z., I. Zak, and R. Freund (1981), Active faulting in the Dead Sea rift, *Tectonophysics*, *80*, 1–26.
- Ginzburg, A., and Z. Ben-Avraham (1997), A seismic refraction study of the north basin of the Dead Sea, Israel, *Geophys. Res. Lett.*, *24*(16), 2063–2066, doi:10.1029/97GL01884.
- Ginzburg, A., J. Makris, K. Fuchs, B. Perathoner, and C. Prodehl (1979), Detailed structure of the crust and upper mantle along the Jordan-Dead Sea Rift, *J. Geophys. Res.*, *84*(B10), 5605–5612, doi:10.1029/JB084iB10p05605.
- Ginzburg, A., M. Reshef, Z. Ben-Avraham, and U. Schattner (2007), The style of transverse faulting in the Dead Sea basin from seismic reflection data: The Amazyahu fault: Israel, *J. Earth Sci.*, *55*(3), 129–139, doi:10.1560/JES_55_3_129.
- Hall, J. K. (1993), The GSI digital terrain model (DTM) project completed, *Curr. Res. Geol.*, *8*, 47–50.
- Hauksson, E., and P. Shearer (2005), Southern California hypocenter relocation with waveform cross-correlation, Part 1: Results using the double-difference method, *Bull. Seismol. Soc. Am.*, *95*(3), 896–903, doi:10.1785/0120040167.
- Hofstetter, A., Y. Gitterman, V. Pinsky, K. Nadia, and L. Feldman (2008), Seismological observations of the northern Dead Sea basin earthquake on 11 February 2004 and its associated activity: Israel, *J. Earth Sci.*, *57*, 101–124, doi:10.1560/JES.57.2.101.
- Hofstetter, A., C. Dorbath, and M. Calò (2012), Crustal structure of the Dead Sea basin from local earthquake tomography, *Geophys. J. Int.*, *189*(1), 554–568.
- Hofstetter, R., Y. Klinger, A. Q. Amrat, L. Rivera, and L. Dorbath (2007), Stress tensor and focal mechanisms along the Dead Sea fault and related structural elements based on seismological data, *Tectonophysics*, *429*(3–4), 165–181, doi:10.1016/j.tecto.2006.03.010.
- Johnson, S. (1967), Hierarchical clustering schemes, *Psychometrika*, *32*(3), 241–254, doi:10.1007/BF02289588.
- Kashai, E. L., and P. F. Croker (1987), Structural geometry and evolution of the Dead Sea Jordan rift system as deduced from new subsurface data, *Tectonophysics*, *141*(1–3), 33–60.
- Katzman, R., U. S. ten Brink, and J. A. Lin (1995), Three dimensional modeling of pull-apart basin: Implications for the tectonics of the Dead Sea Basin, *J. Geophys. Res.*, *100*(B4), 6295–6312, doi:10.1029/94JB03101.
- Kroll, K. A., E. S. Cochran, K. B. Richards-Dinger, and D. F. Sumy (2013), Aftershocks of the 2010 M_w 7.2 El Mayor-Cucapah earthquake reveal complex faulting in the Yuha Desert, California, *J. Geophys. Res. Solid Earth*, *118*, 6146–6164, doi:10.1002/2013JB010529.
- Larsen, B. D., Z. Ben-Avraham, and H. Shulman (2002), Fault and salt tectonics in the southern Dead Sea basin, *Tectonophysics*, *346*(1–2), 71–90, doi:10.1016/S0040-1951(01)00229-3.
- Lazar, M., Z. Ben-Avraham, and U. Schattner (2006), Formation of sequential basins along a strike-slip fault—Geophysical observations from the Dead Sea basin, *Tectonophysics*, *421*(1–2), 53–69, doi:10.1016/j.tecto.2006.04.007.
- Lazar, M., Z. Ben-Avraham, S. Marco, Z. Garfunkel, N. Porat, and Z. Ben-Avraham (2010), Is the Jericho escarpment a tectonic or a geomorphological feature? Active faulting and paleoseismic trenching, *J. Geol.*, *118*(3), 261–276, doi:10.1086/651504.
- Lin, J., and R. S. Stein (2004), Stress triggering in thrust and subduction earthquakes and stress interaction between the southern San Andreas and nearby thrust and strike-slip faults, *J. Geophys. Res.*, *109*, B02303, doi:10.1029/2003JB002607.
- Massa, M., E. Eva, D. Spallarossa, and C. Eva (2006), Detection of earthquake clusters on the basis of waveform similarity: An application in the monferrato region (Piedmont, Italy), *J. Seismol.*, *10*(1), 1–22, doi:10.1007/s10950-006-2840-4.
- Mechie, J., K. Abu-Ayyash, Z. Ben-Avraham, R. El-Kelani, I. Qabbani, and M. Weber (2009), Crustal structure of the southern Dead Sea basin derived from project DESIRE wide-angle seismic data, *Geophys. J. Int.*, *178*(1), 457–478, doi:10.1111/j.1365-246X.2009.04161.x.
- Neev, D., and J. K. Hall (1979), Geophysical investigations in the Dead Sea, *Sediment. Geol.*, *23*(1–4), 209–238, doi:10.1016/0037-0738(79)90015-0.
- Ouillon, G., and D. Sornette (2011), Segmentation of fault networks determined from spatial clustering of earthquakes, *J. Geophys. Res.*, *116*, B02306, doi:10.1029/2010JB007752.
- Reches, Z. (1987), Mechanical aspects of pull-apart basins and push-up swells with applications to the Dead Sea transform, *Tectonophysics*, *141*(1–3), 75–88.
- Reches, Z., and D. F. Hoexter (1981), Holocene seismic and tectonic activity in the Dead Sea area, *Tectonophysics*, *80*(1–4), 235–254.
- Rotstein, Y., Y. Bartov, and A. Hofstetter (1991), Active compressional tectonics in the Jericho area, Dead Sea Rift, *Tectonophysics*, *198*, 239–259, doi:10.1016/0040-1951(91)90153-J.
- Rubinstein, S., I. Barel, Z. Reches, O. Braun, M. Urbakh, and J. Fineberg (2011), Slip sequences in laboratory experiments resulting from inhomogeneous shear as analogs of earthquakes Associated with a Fault Edge, *Pure Appl. Geophys.*, *168*(12), 2151–2166, doi:10.1007/s00024-010-0239-1.
- Segall, P., and D. D. Pollard (1980), Mechanics of discontinuous faults, *J. Geophys. Res.*, *85*(B8), 4337–4350, doi:10.1029/JB085iB08p04337.
- Shalev, E., V. Lyakhovskiy, and Y. Yechieli (2007), Is advective heat transport significant at the Dead Sea basin?, *Geofluids*, *7*(3), 292–300.
- Shalev, E., V. Lyakhovskiy, Y. Weinstein, and Z. Ben-Avraham (2013), The thermal structure of Israel and the Dead Sea Fault, *Tectonophysics*, *602*, 69–77, doi:10.1016/j.tecto.2012.09.011.
- Shapira, A., and A. Hofstetter (2002), Seismicity parameters of seismogenic zones, Israel Geophysical Institute.
- Shapira, A., R. Avni, and A. Nur (1993), New estimate of the Jericho earthquake epicenter of July 11, 1927, *Isr. J. Earth Sci.*, *42*, 93–96.
- Shearer, P. M., J. L. Hardebeck, L. Astiz, and K. B. Richards-Dinger (2003), Analysis of similar event clusters in aftershocks of the 1994 Northridge, California, earthquake, *J. Geophys. Res.*, *108*(B1), 2035, doi:10.1029/2001JB000685.
- Shearer, P., E. Hauksson, and G. Q. Lin (2005), Southern California hypocenter relocation with waveform cross-correlation, Part 2: Results using source-specific station terms and cluster analysis, *Bull. Seismol. Soc. Am.*, *95*(3), 904–915, doi:10.1785/01200401168.
- Smit, J., J.-P. Brun, X. Fort, S. Cloetingh, and Z. Ben-Avraham (2008), Salt tectonics in pull-apart basins with application to the Dead Sea Basin, *Tectonophysics*, *449*(1–4), 1–16, doi:10.1016/j.tecto.2007.12.004.
- Stein, R. S. (1999), The role of stress transfer in earthquake occurrence, *Nature*, *402*, 605–609.
- Stein, R. S., A. A. Barka, and J. H. Dieterich (1997), Progressive failure on the North Anatolian fault since 1939 by earthquake stress triggering, *Geophys. J. Int.*, *128*(3), 594–604, doi:10.1111/j.1365-246X.1997.tb05321.x.
- ten Brink, U. S., and Z. Ben-Avraham (1989), The anatomy of a pull-apart basin - seismic-reflection observations of the Dead Sea basin, *Tectonics*, *8*(2), 333–350, doi:10.1029/TC008i002p00333.

- ten Brink, U. S., and C. H. Flores (2012), Geometry and subsidence history of the Dead Sea basin: A case for fluid-induced mid-crustal shear zone?, *J. Geophys. Res.*, *117*, B01406, doi:10.1029/2011JB008711.
- ten Brink, U. S., Z. Ben-Avraham, R. E. Bell, M. Hassouneh, D. F. Coleman, G. Andreasen, G. Tibor, and B. Coakley (1993), Structure of the Dead Sea pull-apart basin from gravity analysis, *J. Geophys. Res.*, *98*(B12), 21,877–21,894, doi:10.1029/93JB02025.
- ten Brink, U. S., R. Katzman, and J. Lin (1996), Three-dimensional models of deformation near strike-slip faults, *J. Geophys. Res.*, *101*(B7), 16,205–16,220, doi:10.1029/96JB00877.
- ten Brink, U. S., A. S. Al-Zoubi, C. H. Flores, Y. Rotstein, I. Qabbani, S. H. Harder, and G. R. Keller (2006), Seismic imaging of deep low-velocity zone beneath the Dead Sea basin and transform fault: Implications for strain localization and crustal rigidity, *Geophys. Res. Lett.*, *33*, L24314, doi:10.1029/2006GL027890.
- Toda, S., R. S. Stein, K. B. Richards-Dinger, and S. Bozkut (2005), Forecasting the evolution of seismicity in southern California: Animations built on earthquake stress transfer, *J. Geophys. Res.*, *110*, B05S16, doi:10.1029/2004JB003415.
- van Eck, T., and A. Hofstetter (1989), Microearthquake activity in the Dead Sea region, *Geophys. J. Int.*, *99*(3), 605–620, doi:10.1111/j.1365-246X.1989.tb02045.x.
- Waldhauser, F., and W. L. Ellsworth (2000), A double-difference earthquake location algorithm: Method and application to the northern Hayward Fault, California, *Bull. Seismol. Soc. Am.*, *90*(6), 1353–1368.
- Weinberger, Z. B., N. Waldmann, M. Gardosh, G. Baer, A. Frumkin, S. Wdowski, and R. Begin (2006), Quaternary rise of the Sedom diapir, Dead Sea basin, *Geol. Soc. Am.*, *40*, 33–51.
- Wells, D. L., and K. J. Coppersmith (1994), New empirical relationships among magnitude, rupture length, rupture width, rupture area, and surface displacement, *Bull. Seismol. Soc. Am.*, *84*(4), 974–1002.
- Zak, I., R. Freund, and Z. Garfunkel (1981), Asymmetry and basin migration in the Dead Sea rift, *Tectonophysics*, *80*(1–4), 27–38.
- Zaliapin, I., and Y. Ben-Zion (2013), Earthquake clusters in southern California I: Identification and stability, *J. Geophys. Res. Solid Earth*, *118*, 2847–2864, doi:10.1002/jgrb.50179.